Propagation of data-modulated Gaussian beams through holographic optical elements

Jing M. Tsui*, **Charles Thompson***, **and Jeffrey M. Roth**†

*Department of Electrical and Computer Engineering, University of Massachusetts – Lowell, 1 University Ave., Lowell, MA, USA 01854

†MIT Lincoln Laboratory, 244 Wood St., Lexington, MA USA 02420

jroth@ll.mit.edu

Abstract: This paper examines dispersion caused by diffraction through uniform volume holographic gratings. Of interest is the impact of this dispersion on the spatial and temporal fidelity of an optical communications signal. To this end, a holographic grating is illuminated by a Gaussian beam with $1/e^2$ diameter large compared to the optical wavelength. Coupled-wave analysis is used to calculate the temporal response of the grating to transmitted symbols encoded in time as a train of Gaussian-shaped pulses. It is shown that temporal dispersion due to diffraction impacts bit-error performance, yielding increased power penalty for larger diffraction angles and beam diameters.

OCIS codes: (090.2890) Holographic optical elements; (090.7330) Volume holographic gratings; (060.4510) Optical communications; (050.1755) Computational electromagnetic methods; (260.2110) Electromagnetic optics; (050.1950) Diffraction gratings.

References and links

1. G. B. Venus, A. Sevian, V. I. Smirnov, and L. B. Glebov, "Stable coherent coupling of laser diodes by a volume Bragg grating in photothermorefractive glass," Opt. Lett. **31**, 1453–1455 (2006).
2. J. Lumeau, L. B. Glebov, and V. Smirnov, "Tunable narrowband filter based on a combination of Fabry-Perot etalon and volume Bragg grating," Opt. Lett. **31**, 2417–2419 (2006).
3. J.-P. Herriau, A. Delboulbé, J.-P. Huignard, G. Roosen, and G. Pauliat, "Optical-Beam Steering for Fiber Array Using Dynamic Holography," J. Lightwave Technol. **LT-4**, 905–907 (1986).
4. M. G. Moharam and T. K. Gaylord, "Rigorous coupled-wave analysis of planar-grating diffraction," J. Opt. Soc. Am. **71**, 811–818 (1981).
5. J. M. Tsui, C. Thompson, V. Mehta, J. M. Roth, V. I. Smirnov, and L. B. Glebov, "Coupled-wave analysis of apodized volume gratings," Opt. Express **12**, 6642–6653 (2004).
6. S.-D. Wu, T. K. Gaylord, E. N. Glytsis, and Y.-M. Wu, "Three-dimensional converging-diverging Gaussian beam diffraction by a volume grating," J. Opt. Soc. Am. A **22**, 1293–1304 (2005).
7. C. S. Williams, "Gaussian Beam Formulas from Diffraction Theory," Appl. Opt. **12**, 872–876 (1973).
8. H. G. Kraus, "Huygens-Fresnel-Kirchhoff wave-front diffraction formulation: paraxial and exact Gaussian laser beams," J. Opt. Soc. Am. A **7**, 47–65 (1990).
9. P. M. Morse and H. F. Feshbach, *Methods of Theoretical Physics* (McGraw-Hill Book Company, Inc., New York, 1953).
10. L. G. Kazovsky and O. K. Tonguz, "Sensitivity of Direct-Detection Lightwave Receivers Using Optical Preamplifiers," IEEE Photon. Technol. Lett. **3**, 53–55 (1991).
11. P. A. Humblet and M. Azizoğlu, "On the Bit Error Rate of Lightwave Systems with Optical Amplifiers," J. Lightwave Technol. **9**, 1576–1582 (1991).

#106187 - $15.00 USD Received 9 Jan 2009; revised 20 Feb 2009; accepted 3 Mar 2009; published 24 Mar 2009

1. Introduction

The development of photo-thermo-refractive glass (PTRG) [1,2] has enabled a number of key performance enhancements in holographic optical elements (HOEs). Improvements include higher diffraction efficiency, lower loss, high-power handling, stability under radiation and temperature, and larger (∼1 – 2-in) diameters. These advantages have opened up new applications for PTRG-based HOEs in wavelength combining [1], spectral filtering [2], and beam-steering applications [3].

When used in a communications system, an HOE must transmit symbols represented by a temporal waveform with high fidelity. However, HOEs, like all Bragg-diffraction devices, lack true-time delay. An optical beam passing through an HOE experiences variable time delay across the beam's transverse dimension, changing the temporal characteristics of the transmitted pulse in the plane of diffraction. This distortion-producing effect may be significant in applications requiring appreciable aperture diameters and diffraction angles, for example in high-data-rate, diffraction-based, beam-steering techniques for free-space-optical communications [3]. In this application, an HOE may be used to steer a light beam, allowing connectivity between two terminals.

The two-dimensional schematic of the problem's geometry is shown in Fig. 1. The incident beam exhibits a Gaussian profile in space and time, and diffraction occurs only in the x-z plane. To achieve high diffraction efficiency, the input beam must have a narrow spatial bandwidth with low angular divergence. On the other hand, as the beam diameter increases, the time-delay effects become more pronounced. For a specific application, a tradeoff can be considered between high diffraction efficiency from using a large beam diameter, and reduced diffraction dispersion from using a narrow beam diameter.

In this paper we examine the dependence of wave propagation through an HOE on spatial and temporal features of the incident beam. We assess the impact of non-true-time-delay dispersion on a communications signal by analyzing bit-error-ratio performance at the receiver. This paper presents a derivation of the coupled-wave equations and boundary conditions for a two-dimensional incident beam in Sections 3 and 4. The results for a Gaussian incident beam with $1/e^2$ beam diameters ranging from 5 to 40 mm are presented in Section 5. In Section 6 we describe the model for the bit-error-ratio simulations, and the simulation results are presented in Section 7. A summary and conclusions are given in Section 8.

2. Volume holograms

A uniform HOE has a sinusoidally-modulated relative permittivity $\epsilon(\bar{x})$ given by

$$\epsilon(\bar{x}) = \epsilon_{20} + \epsilon_{21} \cos\left[\bar{K} \cdot \bar{x}\right], \tag{1}$$

where $\bar{x}$ is the position vector, $\bar{K}$ is the grating vector, and where $\bar{K} = K[\sin\phi \ 0 \ \cos\phi]^T$. The angle ϕ is the grating slant angle (shown in Fig. 1) defined with respect to the z-axis in the x-z-plane. The quantities ϵ_{20} and ϵ_{21} denote the mean permittivity and modulation amplitude, respectively.

As shown in Fig. 1, Regions 1 and 3 have free-space properties, while Region 2 represents the holographic grating. The z-axis is perpendicular to the surface of the grating and is in the plane of propagation. The media interfaces are perpendicular to the z-axis, with the x-axis in the plane of the page and the y-axis normal to the page. The wave from Region 1 strikes the interface at incident angle θ_1 satisfying the Bragg condition, causing reflection and transmission into Regions 1 and 2, respectively. We denote the scattering angles as θ_{r_m}, where r is the region number and m is the integral index of the m^{th} spatial harmonic. In Region 2, the beam can diffract forward into Region 3 or backward into Region 1.

#106187 - $15.00 USD Received 9 Jan 2009; revised 20 Feb 2009; accepted 3 Mar 2009; published 24 Mar 2009

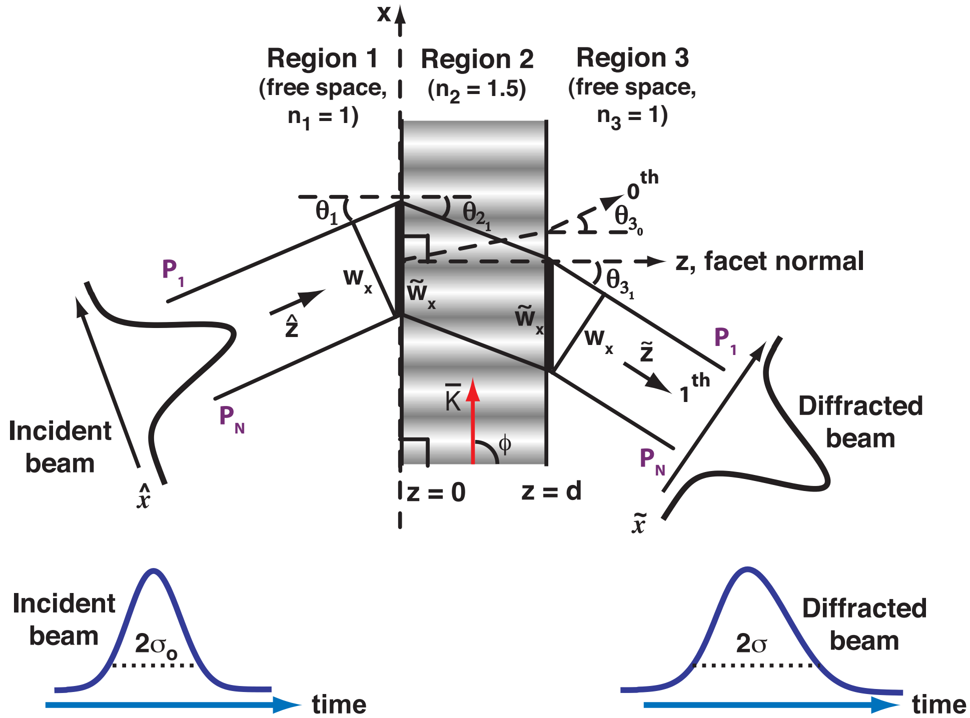

Fig. 1. Schematic of the HOE. The diffraction orders are denoted by subscripts. $\hat{x}$ and $\tilde{x}$ are the incident and output spatial beam dimensions, respectively. The refractive indexes are $n_1 = n_3 = 1$.

HOEs are not-true-time-delay devices, because as Fig. 1 shows the diffracted rays of the beam travel paths of unequal distance in the $\tilde{x}$-$\tilde{z}$ plane. Light traveling path P_1 requires a longer propagation time than light traveling along path P_N, leading to temporal distortions on the transmitted temporal pulse.

The forward and backward propagating diffracted fields that result from an incident plane wave have been examined using the coupled-wave equations approach by Gaylord and Moharam [4], and recently by Tsui et.al [5]. The electric field inside the grating is expressed as a superposition of elemental waves having spatial wavenumber harmonics $\bar{k}_{2m}$, and amplitudes $A_m(k_x, k_y, z)$. We are interested in accurately computing the forward- and backward-propagating diffracted fields resulting from the incident beam directed at oblique incidence on the volume grating. This analysis also requires computing the temporal response of the grating. Fig. 1 shows the configuration of a beam at an arbitrary incident angle θ_1.

Three-dimensional, coupled-wave analysis of Gaussian incident beams has been applied to planar gratings to consider beam-divergence effects [6]. In our analysis, we consider general spatially-varying incident beam profiles with H-mode polarization, retaining the temporal domain. The solution applies to a range of spatial profiles, including Gaussian beams. We derive the coupled-wave equations and state the boundary-condition requirements. The incident beam is taken to be collimated. The solution of the electric field inside the grating (Region 2) is calculated by matching spatial harmonic modes at the grating interface for each spatial wavenumber.

3. Coupled-wave analysis and boundary conditions for incident beam

The incident wave in Region 1 is expressed as a function of the coordinates $(\hat{x}, y, \hat{z})$, where the propagation direction is collinear to the $\hat{z}$–axis. The diffracted wave in Region 3 is expressed as a function of the coordinates $(\tilde{x}, y, \tilde{z})$. The two coordinate systems are related to the $x-z$ system through coordinate transformations shown in Fig. 2. The expressions for $\hat{x}$, $\hat{z}$, $\tilde{x}$ and $\tilde{z}$ as

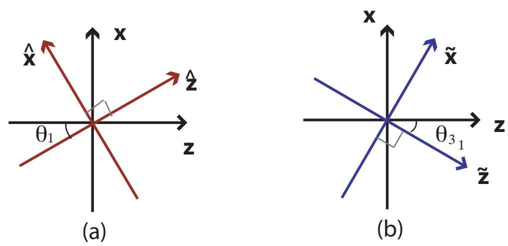

Fig. 2. Diagram of axes rotations for input (a) and output (b) beams.

functions of x and z are shown in the the unitary-transformation matrixes of Eqs. (2) and (3), where $S_1 = \sin\theta_1$, $C_1 = \cos\theta_1$, $S_{3_1} = \sin\theta_{3_1}$ and $C_{3_1} = \cos\theta_{3_1}$.

$$\begin{bmatrix} \hat{x} \\ \hat{z} \end{bmatrix} = \begin{bmatrix} C_1 & -S_1 \\ S_1 & C_1 \end{bmatrix} \begin{bmatrix} x \\ z \end{bmatrix} \tag{2}$$

$$\begin{bmatrix} \tilde{x} \\ \tilde{z} \end{bmatrix} = \begin{bmatrix} C_{3_1} & S_{3_1} \\ -S_{3_1} & C_{3_1} \end{bmatrix} \begin{bmatrix} x \\ z \end{bmatrix} \tag{3}$$

The complex amplitude of the temporal Fourier transform of the y-directed electric field, $\mathcal{E}_{n_y}(\bar{x}, \omega)$, is assumed to be uniform in the y-direction and n is the region number. The resultant scalar Helmholtz wave equation for H-mode polarization is

$$\nabla^2 \mathcal{E}_{n_y}(\bar{x}, \omega) + k_o^2 \mu \epsilon(\bar{x}) \mathcal{E}_{n_y}(\bar{x}, \omega) = 0, \tag{4}$$

where $k_o^2 = \omega^2 \mu_o \epsilon_o$ and μ_o and ϵ_o are the permeability and permittivity in vacuum, respectively. The parameters μ and ϵ are the respective relative permeability and permittivity of the medium.

The total incident electric field, $e_{1_{y_i}}$, can be expressed in terms of its spatial ($\bar{k}$) and angular (ω) frequencies Fourier transform as shown below.

$$e_{1_{y_i}}(\bar{\hat{x}}, t) = \left(\frac{1}{2\pi}\right)^3 \iiint E_{1_{y_i}}(\bar{\hat{x}}, \bar{k}, \omega) e^{j\omega t} dk_x\, dk_y\, d\omega \tag{5}$$

$E_{1_{y_i}}$ represents the incident electric field for a given spatial frequency and location:

$$E_{1_{y_i}}(\bar{\hat{x}}, \bar{k}, \omega) = \mathsf{E}(k_x, k_y, \omega) e^{-jk_x\hat{x}} e^{-jk_y y} e^{-j\sqrt{k_1^2 - k_x^2 - k_y^2}\,\hat{z}}. \tag{6}$$

The incident field is a sum of all the spatial frequencies k_x and k_y. This applies to the electric field in all regions. Using the coordinate transformation given in Eq. (2), the incident-wave beam is expressed as a function of coordinates x and z. The beam $\mathcal{E}_{3_y}(\bar{x}, \omega)$, transmitted from the HOE at $z = d$, is calculated by taking the inverse spatial Fourier transform of the response $T_m(k_x, k_y, \omega)\mathsf{E}(k_x, k_y, \omega)$. The coordinate transformation given in Eq. (3) is used to express the output beam in terms of coordinates $\tilde{x}$ and $\tilde{z}$.

#106187 - $15.00 USD Received 9 Jan 2009; revised 20 Feb 2009; accepted 3 Mar 2009; published 24 Mar 2009

The solution for the electric field inside the HOE, E_{2_y}, satisfying Eq. (4) can be expressed in terms of an infinite series where the coefficients of the series satisfy the following coupled-wave equation [4,5]:

$$E_{2_y} = \sum_{m=-\infty}^{+\infty} \mathsf{E}(k_x,k_y,\omega)A_m(k_x,k_y,z,\omega)e^{-j\Psi_m(x,z)}e^{-jk_y y}. \tag{7}$$

For simplicity $\Psi_m(x,z)$ is expressed as Ψ_m. Upon substitution of Eq. (7) into Eq. (4), the coupled-wave equations governing the complex amplitude A_m become

$$\begin{aligned} \frac{\partial^2 A_m}{\partial z^2} &- 2j\left[mk_x\hat{C} - k_x S_2 + \sqrt{k_2^2 - k_x^2 - k_y^2}C_2\right]\frac{\partial A_m}{\partial z} \\ &- 2mK\left[\frac{mK}{2} + k_x\sin(\phi-\theta_2) + \sqrt{k_2^2-k_x^2-k_y^2}\cos(\phi-\theta_2)\right]A_m \\ &+ \frac{k_2^2\epsilon}{2}A_{m+1} + \frac{k_2^2\epsilon}{2}A_{m-1} = 0, \end{aligned} \tag{8}$$

where $k_2 = k_o n_2$. $\hat{S} = \sin\phi$ and $\hat{C} = \cos\phi$. The spatial harmonics, Ψ_m, are parameterized by Eq. (9).

$$\Psi_m = \Psi_0 + mK\left(\hat{S}\,x + \hat{C}z\right) \tag{9}$$

Ψ_0 represents the spatial harmonic for $m = 0$ and $\Psi_0 = \hat{x}k_x + \hat{z}\sqrt{k_2^2 - k_x^2 - k_y^2}$. Using the axes transformation shown in Eq. (2), the spatial harmonic for the 0^{th} order is expressed as a function of x and z as shown below.

$$\Psi_0 = k_x[C_2x - S_2z] + \sqrt{k_2^2 - k_x^2 - k_y^2}\,[S_2x + C_2z] \tag{10}$$

We define $S_2 = \cos\theta_{2_0}$ and $C_2 = \sin\theta_{2_0}$. θ_{2_0} is the zero-order ($m = 0$) diffracted angle inside the grating.

The electric field in Region 1, E_{1_y}, can be expressed as the sum of the incident wave $E_{1_{y_i}}$, and the reflected wave $E_{1_{y_r}}$, which is $E_{1_y} = E_{1_{y_i}} + E_{1_{y_r}}$. The incident and reflected waves in Region 1 are expressed in Eqs. (11) and (12), respectively. The solution of the electric field for Region 3, following a similar form to Regions 1 and 2, is expressed in Eq. (13).

$$E_{1_{y_i}} = \mathsf{E}(k_x,k_y,\omega)e^{-jk_x[C_1x-S_1z]}e^{-j\sqrt{k_1^2-k_x^2-k_y^2}[S_1x+C_1z]}e^{-jk_y y} \tag{11}$$

$$E_{1_{y_r}} = \mathsf{E}(k_x,k_y,\omega)R_m(k_x,k_y,\omega)e^{-j\left[k_xC_r+\sqrt{k_1^2-k_x^2-k_y^2}S_r-mK\hat{S}\right]x}e^{-jk_y y}e^{j\gamma_{1_m}z} \tag{12}$$

$$\begin{aligned} E_{3_y} = \mathsf{E}(k_x,k_y,\omega)T_m(k_x,k_y,\omega)e^{-j\left[k_xC_3+\sqrt{k_3^2-k_x^2-k_y^2}S_3-mK\hat{S}\right]x}e^{-jk_y y} \times \\ e^{-j\gamma_{3_m}(z-d)}e^{-j(\Psi_0+mK\hat{C})d} \end{aligned} \tag{13}$$

In the above expressions, $k_1 = k_o n_1$ and $k_3 = k_o n_3$. In addition, $C_r = \cos\theta_r$, $S_r = \sin\theta_r$, θ_r is the reflection angle for spatial mode $m = 0$, $S_3 = \sin\theta_{3_0}$, and $C_3 = \cos\theta_{3_0}$. The parameter γ_{n_m} is the wavenumber in Region n for mode m.

Continuity in the trace wavenumber along the boundaries $z = 0$ and $z = d$ (respectively) yields conditions

$$k_xC_1 + S_1\sqrt{k_1^2-k_x^2-k_y^2} = k_xC_r + S_r\sqrt{k_1^2-k_x^2-k_y^2}, \tag{14}$$

$$k_xC_1 + S_1\sqrt{k_1^2-k_x^2-k_y^2} = k_xC_2 + S_2\sqrt{k_2^2-k_x^2-k_y^2} = k_xC_3 + S_3\sqrt{k_3^2-k_x^2-k_y^2}. \tag{15}$$

#106187 - $15.00 USD Received 9 Jan 2009; revised 20 Feb 2009; accepted 3 Mar 2009; published 24 Mar 2009

Therefore, $\theta_r = \theta_1$. For $k_3 = k_1$ the angle $\theta_1 = \theta_{3_0}$. The angles of the backward- and forward-propagating diffracted waves are calculated using $k_{1_m}\sin\theta_{1_m} = k_{2_m}\sin\theta_{2_m} = k_{3_m}\sin\theta_{3_m}$. If the reflected and diffracted waves in Regions 1 and 3 are to satisfy the Helmholtz wave equation, γ_{1_m} and γ_{3_m} must satisfy the dispersion relations shown in Eqs. (16) and (17).

$$\gamma_{1_m}^2 = k_1^2 - \left\{k_x C_r + S_r\sqrt{k_1^2 - k_x^2 - k_y^2} - mK\hat{S}\right\}^2 \tag{16}$$

$$\gamma_{3_m}^2 = k_3^2 - \left\{k_x C_3 + S_3\sqrt{k_1^2 - k_x^2 - k_y^2} - mK\hat{S}\right\}^2 \tag{17}$$

The quantities R_m in Eq. (12) are amplitudes of backward-propagating diffracted orders, and T_m in Eq. (13) are amplitudes of forward-propagating orders. These amplitudes are specified by the boundary conditions. At the boundaries $z = 0$ and $z = d$, the tangential components of the electric and magnetic fields are continuous. For each value of m, the continuity of the tangential electric and magnetic fields at $z = 0$ and $z = d$ yields the relations below.

$$(\bar{E})_t(z=0): \qquad R_m - A_m = \delta_{m0} \tag{18}$$

$$(\bar{H})_t(z=0): \qquad j\gamma_{1_m} R_m - \frac{\partial A_m}{\partial z} + j\frac{\partial \Psi_m}{\partial z}A_m = j\delta_{m0}\left(-kS_1 + \sqrt{k_1^2 - k_x^2 - k_y^2}\,C_1\right) \tag{19}$$

$$(\bar{E})_t(z=d): \qquad A_m - T_m = 0 \tag{20}$$

$$(\bar{H})_t(z=d): \qquad \frac{\partial A_m}{\partial z} - \frac{\partial \Psi_m}{\partial z}A_m + j\gamma_{3_m}T_m = 0 \tag{21}$$

4. Transmitted and reflected waveform

In this section we describe our approach to obtain the transmitted and reflected fields in Regions 1 and 3. In these regions, Huygens' principle is used to assemble the electric fields, whereas the coupled wave equation is used in Region 2. Huygens' principle has been used previously for wave-front propagation and diffraction calculations [7–9].

The solution of the wave equation $f(\bar{x}, t)$ can be expressed as the integral given in Eq. (22), where $\int(\cdot)dS_o$ is a surface integral.

$$f(\bar{x}, t) = \int dt_o \int dS_o \left[f\,\frac{\partial g}{\partial z_o}\right] \tag{22}$$

The normal derivative of the Green's function is

$$\frac{\partial g}{\partial z_o} = \frac{1}{2\pi}\frac{z}{R}\left[\frac{\delta(R/c - t + t_o)}{R^2} + \frac{\partial}{\partial t_o}\frac{\delta(R/c - t + t_o)}{Rc}\right] \tag{23}$$

The function $\delta(\cdot)$ is the Dirac delta function and c is the phase velocity in Regions 1 and 3. The distance $R = |\bar{x} - \bar{x}_o|$ is equal to the distance between the source and observation points. The solution for $f(\bar{x}, t)$ external to the HOE is expressed in terms of the surface field at the HOE boundaries:

$$f(\bar{x}, t) = \frac{1}{2\pi}\int dS_o \cos\vartheta\left[\frac{f\left(\bar{x}_o, t - \frac{R}{c}\right)}{R^2} + \frac{1}{Rc}\frac{\partial f(\bar{x}_o, t_o)}{\partial t_o}\Big|_{t_o = t - \frac{R}{c}}\right], \tag{24}$$

where $\cos\vartheta = \frac{z}{R}$.

#106187 - $15.00 USD Received 9 Jan 2009; revised 20 Feb 2009; accepted 3 Mar 2009; published 24 Mar 2009

5. Numerical solution for a Gaussian beam traveling through a uniform volume grating

In this section, we discuss the results of the output beam calculated by the method developed in the previous sections. The incident wave is a two-dimensional beam with axes $\hat{x}$ and y, and propagation direction $\hat{z}$. We assume the incident wave is separable in spatial coordinates. Fig. 3 shows a block diagram of the incident wave propagation sequence from Region 1 to 2, and then to Region 3. The results shown in this section represent the case of a two-dimensional Gaussian beam temporally modulated by a Gaussian pulse. The beam's modulation waveform is given by the function $\hat{p}(t)$.

Using the axes transformation shown in Eq. (2), the incident beam is expressed as a function of x and z. In Region 1 at $z = -z_1$, the spatial and temporal Fourier transforms of the incident beam, $E(\bar{k},\omega)$, are written as follows:

$$\begin{aligned} \mathsf{E}(k_x,k_y,\omega) &= \iiint g_{ix}(\hat{x})g_{iy}(y)\hat{p}_i(t)e^{jk_y y}e^{jk_x\hat{x}}e^{-j\omega t}\, d\hat{x}\, dy\, dt \\ &= G_{ix}(k_x)G_{iy}(k_y)\hat{p}(\omega) \end{aligned} \tag{25}$$

$G_{ix}(k_x)$, $G_{iy}(k_y)$ and $\hat{P}(\omega)$ are the Fourier transform of g_{ix}, g_{iy} and $\hat{p}(t)$, respectively. The $1/e^2$ spatial widths of the Gaussian beam are w_x and w_y, and σ_o is the $1/e^2$ width of the Gaussian temporal pulse. The Gaussian pulse is modulated at center frequency $\omega_o = \frac{2\pi c}{\lambda_o}$. The input pulse waveform is given by $\hat{p}_i(t) = p_i(t)\cos(\omega_o t)$, where the pulse center is μ_t.

$$g_{ix} = e^{-\left(\frac{\hat{x}}{w_x}\right)^2} \tag{26}$$

$$g_{iy} = e^{-\left(\frac{y}{w_y}\right)^2} \tag{27}$$

$$p_i(t) = = e^{-\frac{(t-\mu_t)^2}{\sigma_o^2}} \tag{28}$$

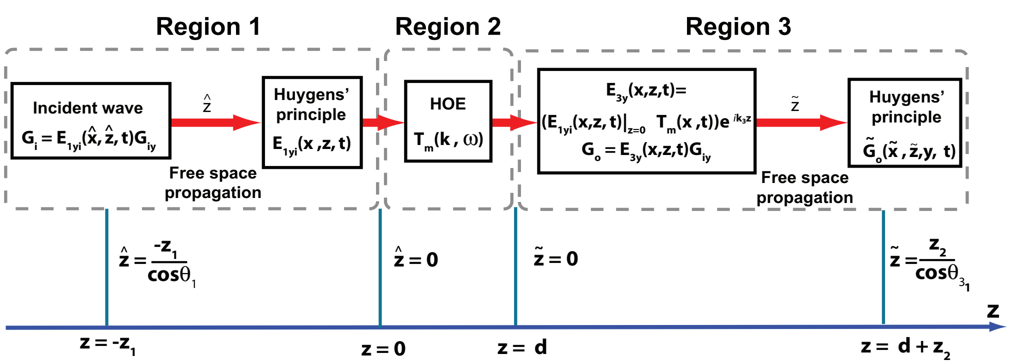

Fig. 3. Block diagram for numerical simulation of Gaussian beam propagating through a holographic optical element.

A single volume grating produces one-dimensional diffraction, which in our case occurs in the x-direction. No diffraction occurs in the y-direction. Therefore, R_m, A_m and T_m are only functions of k_x and z. $T_m(k_x,k_y,\omega)$ is the Fourier transform ($\omega = \frac{2\pi c}{\lambda}$) of the impulse response of the volume grating for the forward-propagating diffracted wave at $z = d$. The spatial

#106187 - $15.00 USD Received 9 Jan 2009; revised 20 Feb 2009; accepted 3 Mar 2009; published 24 Mar 2009

spectrum of an incident Gaussian beam with different $1/e^2$ beam diameters ($2w_x = 2w_y$), $G_{ix}(k_x) = G_{iy}(k_y)$, and the spatial spectrum of the first order diffracted wave of the HOE $T_1(k_x, 0, \omega_o)$ and $T_1(0, k_y, \omega_o)$ at center wavelength λ_o are shown in Fig. 4. The x-axis is the normalized spatial wavenumber by subtracted the center wavenumber. For the beam diameter $2w_x = 0.5$ mm, the spatial spectrum, E is broader than the main lobe of the HOE spectrum. To achieve high diffraction efficiency for this HOE geometry, the diameter of the beam ($2w_x$) needs to exceed approximately 1 mm. the amplitude of the T_m for a fixed value of k_x essentially remains constant as k_y varies.

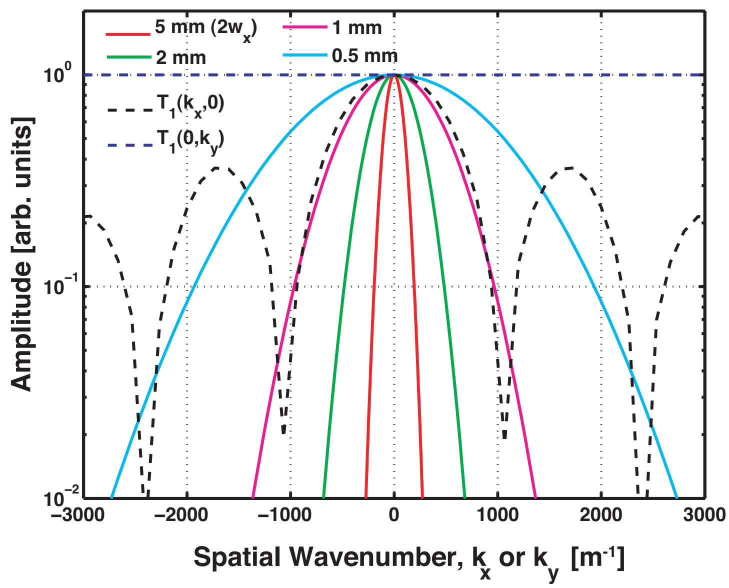

Fig. 4. The spatial spectrum of the first-order, forward-propagating diffracted wave for the Gaussian incident beam at $z = d$. The different solid curves are for different $1/e^2$ beam diameters ($2w_x$). T_1 is the amplitude of the first-order, forward-diffracted beam, plotted along different components of the spatial wavenumber. For high diffraction efficiency, the spatial frequency content of the beam should be well-contained within the HOE spectrum, T_1. Grating period: $\Lambda = 1420$ nm; grating thickness: $d = 1.125$ mm; optical wavelength: $\lambda_o = 1550$ nm.

The spatial spectrum of the HOE for the uniform grating (T_1 in Fig. 4) for a fixed value of k_y is spectrally limited in bandwidth. The $1/e^2$ diameter of the incident beam ($2w_x$, $2w_y$) has a lower bound imposed by the grating's narrow spatial bandwidth of the grating. HOE diffraction depend on the grating period and the wavelength, determined by the Bragg condition. For a fixed center wavelength λ_o, the first-order diffraction angle decreases as the grating period increases. The spatial bandwidth of the grating is affected by the grating period Λ. The 3-dB spatial bandwidth of the HOE increases as the grating period increases. The 3-dB time-frequency bandwidth of the HOE also increases with grating period, reducing the wavelength selectivity of the device. The plot in Fig. 5 shows spatial and spectral 3-dB bandwidths for the HOE. In this application, the value of the spatial width ($2w_x$, $2w_y$) of the Gaussian beam (over diameters of 5 to 40 mm) is much greater than the value of the center wavelength λ_o (1550 nm). Therefore, the relations $k_x \ll k_2$ and $k_y \ll k_2$ hold. These relations apply also to the wavenumbers in Regions 1 and 3, where $k_x \ll k_1$, $k_x \ll k_3$, $k_y \ll k_1$ and $k_y \ll k_3$. For small

#106187 - $15.00 USD Received 9 Jan 2009; revised 20 Feb 2009; accepted 3 Mar 2009; published 24 Mar 2009

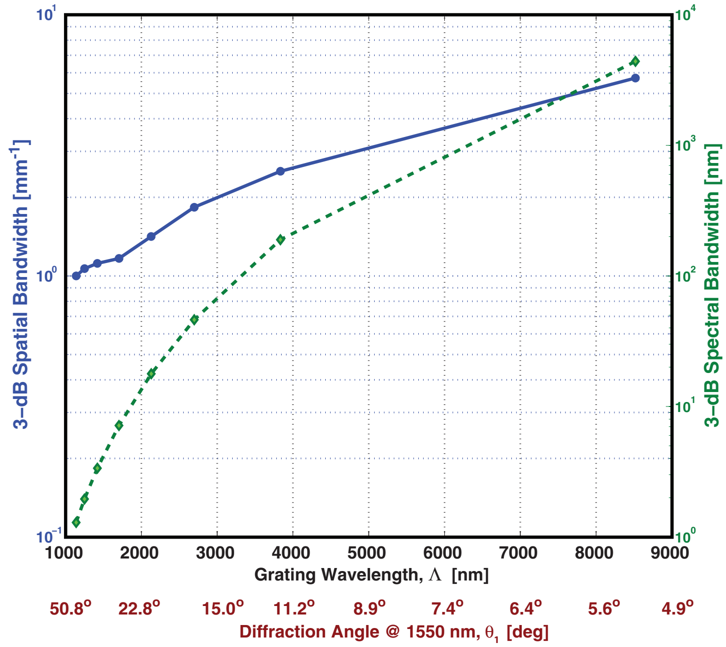

Fig. 5. The 3-dB spatial and spectral (time-frequency) bandwidth of the volume grating designed for optical wavelengths in the 1550-nm band. Horizontal axis given in both grating wavelength and diffraction angle.

changes in k_x and k_y compared to the wavenumber, we make the following approximation:

$$\sqrt{k_n^2 - k_x^2 - k_y^2} \approx \sqrt{k_n^2 - k_x^2} \tag{29}$$

where $n = 1, 2, 3$. Due to the spatial bandwidth of the incident beam we may assume that $k_2 >> k_x$. Hence the solution of S_2 in Eq. (30):

$$\sin(\theta_2) \approx \sin(\theta_o) \quad + \quad \beta\cos(\theta_o), \tag{30}$$

$$\text{where, } \sin(\theta_o) = \sqrt{\frac{k_1^2 - k_x^2}{k_2^2 - k_x^2}} S_1, \quad \text{and} \quad \beta = \frac{k_x(C_1 - \cos(\theta_o))}{\sqrt{k_2^2 - k_x^2}\cos(\theta_o)}.$$

We then approximate the electric fields in the Regions 1, 2 and 3 using Eqs. (31 – 34).

$$\begin{aligned} e_{1_{y_i}}(\bar{x},t) &= \left(\frac{1}{2\pi}\right)^3 \int_{-\infty}^{+\infty} G_{iy}(k_y))e^{-jk_y y} dk_y \iint_{-\infty}^{+\infty} G_{ix}(k_x)\hat{P}(\omega) e^{-jk_x[C_1 x - S_1 z]} e^{-j\sqrt{k_1^2 - k_x^2}[S_1 x + C_1 z]} dk_x e^{j\omega t} d\omega \\ &= g_{iy}\left(\frac{1}{2\pi}\right)^2 \iint_{-\infty}^{+\infty} G_{ix}(k_x)\hat{P}(\omega) e^{-jk_x[C_1 x - S_1 z]} e^{-j\sqrt{k_1^2 - k_x^2}[S_1 x + C_1 z]} dk_x e^{j\omega t} d\omega \end{aligned} \tag{31}$$

$$e_{1_{y_r}}(\bar{x},t) = g_{iy}\left(\frac{1}{2\pi}\right)^2 \iint_{-\infty}^{+\infty} \sum_{m=-\infty}^{+\infty} G_{ix}(k_x)\hat{P}(\omega) R_m(k_x,\omega) e^{-j\left[k_x C_r + \sqrt{k_1^2 - k_x^2} S_r - mK\hat{S}\right]x} e^{j\gamma_{1m} z} e^{j\omega t} dk_x d\omega \tag{32}$$

$$e_{2_y}(\bar{x},t) = g_{iy}\left(\frac{1}{2\pi}\right)^2 \iint_{-\infty}^{+\infty} \sum_{m=-\infty}^{+\infty} G_{ix}(k_x)\hat{P}(\omega) A_m(k_x,z,\omega) e^{-j\Psi_m(x,z)} e^{j\omega t} dk_x d\omega \tag{33}$$

#106187 - $15.00 USD Received 9 Jan 2009; revised 20 Feb 2009; accepted 3 Mar 2009; published 24 Mar 2009

$$e_{3_y}(\bar{x},t) = g_{iy}\left(\frac{1}{2\pi}\right)^2 \iint_{-\infty}^{+\infty} \sum_m G_{ix}(k_x)\hat{P}(\omega)T_m(k_x,\omega)e^{-j\left[k_xC_3+\sqrt{k_3^2-k_x^2}S_3-mK\hat{S}\right]x} \times e^{-j\gamma_{3m}(z-d)}e^{-j(\Psi_0+mK\hat{C})d}e^{j\omega t}dk_xd\omega \tag{34}$$

This approximate model is simpler and requires less computation time than the exact model shown in Section 3. A comparison of the approximate and exact models is shown in Fig. 6 for an incident beam diameter $w_x = w_y = 10$ mm. As expected, using T_1 from the approximate model produces a nearly perfect match to the rigorous model.

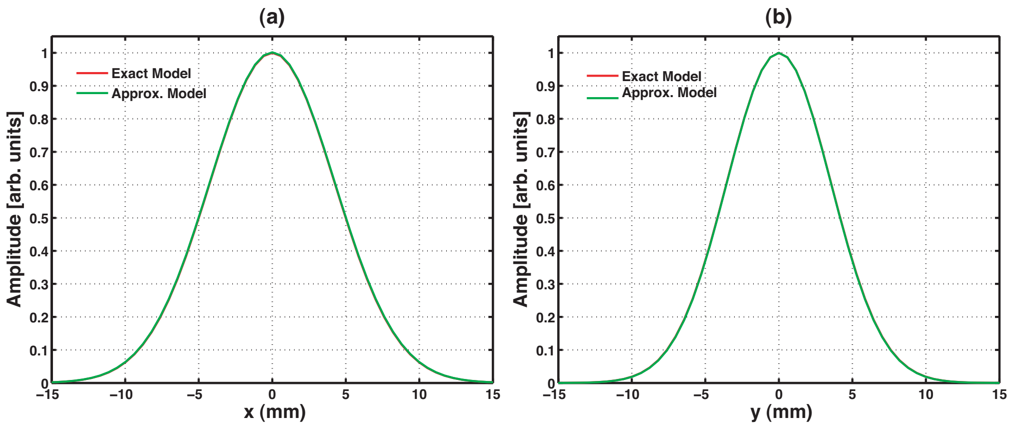

Fig. 6. Comparison of approximate model (Eqs. (32 – 34)) and exact model (Eqs. (7, 12 – 13)): (a) $\mathcal{E}_{3_y}(x,0,d,\omega_o)$ as a function of x at $y=0$, (b) $\mathcal{E}_{3_y}(0,y,d,\omega_o)$ as a function of y at $x = 0$, $w_x = w_y = 10$mm. Both models match very closely.

The incident beam propagates along the $\hat{z}$-direction from $z = -z_1$ to Regions 1/2 boundary at $z = \hat{z} = 0$. To satisfy the parallel beam assumption, the source is near the volume grating. In our simulation, the value of z_1 is chosen to be $z_1 = 10w_x$. $e_{1_{y_i}}(\bar{x},t)|_{z=0}$ is calculated using Huygens' principle in Eq. (24). The incident beam $e_{1_{y_i}}(\bar{x},t)|_{z=-z_1}$ is the function $f(\bar{x}_o,t)$ in the integrand of Eq. (24). Huygens' principle is also used to calculate the output beam in Region 3 propagating along $\tilde{z}$, with wave front in the $\tilde{x}$-y plane. In this case, the output beam $e_{3_y}(\bar{x},t)|_{z=d}$ is the function $f(\bar{x}_o,t)$ in the integrand of Eq. (24). $\hat{p}_i(t)$ is the temporal Gaussian input pulse with carrier frequency modulation at ω_o. From Eq. (24), the second term of the equation inside the surface integral is the partial time derivative of $e_{1_{y_i}}(\bar{x},\ t)$, shown in Eq. (35).

$$\frac{\partial e_{1_{y_i}}(\bar{x},t)}{\partial t} = g_{ix}g_{iy}\left(\frac{dp_i(t)}{dt}\cos(\omega_o t) + \omega_o p_i(t)\cos(\frac{\pi}{2}+\omega_o t)\right) \tag{35}$$

We consider only the temporal pulse envelope by removing the carrier frequency when applying Huygens' principle. Also, the value of ω_o is large, and since the time derivative of $\hat{p}(t)$ is dominated by the second term of Eq. (35), so $\frac{d\hat{p}_i(t)}{dt} \approx p_i(t)\omega_o$, and Eq. (24) is rewritten as

$$\begin{bmatrix} e_{1_{y_i}}(\bar{x},t) \\ e_{3_y}(\bar{x},t) \end{bmatrix} \approx \frac{1}{2\pi}\int dS_o \cos\vartheta\left(\frac{1}{R^2}+\frac{\omega_o}{Rc}\right)\begin{bmatrix} e_{1_{y_i}}\left(\bar{x}_o,t-\frac{R}{c}\right) \\ e_{3_y}\left(\bar{x}_o,t-\frac{R}{c}\right) \end{bmatrix}. \tag{36}$$

The output in Region 3, denoted $e_{3_y}^{(L)}$, is demodulated by passing through a low-pass filter. Using the axes transformation shown in Eq. (3), we have the output beam $e_{3_y}^{(L)}(\bar{\tilde{x}},\ t)$ at $z = d + z_2$.

After integrating over the area of the beam, we have the demodulated pulse, $p_o(t)$. The output beam, $\left\langle e_{3_y}^{(L)}(\tilde{x},\tilde{z},\tau_{max})\right\rangle_y$ at $\tilde{z} = \frac{z_2}{\cos\theta_{3_1}}$ is calculated by integrating along the y-axis. τ_{max} is chosen as the peak value of $p_o(t)$ from Fig. 7. The amplitude of $\left\langle e_{3_y}^{(L)}(\tilde{x},\tilde{z},\tau_{max})\right\rangle_y$ at $\tilde{z} = \frac{z_2}{\cos\theta_{3_1}}$ is normalized for comparing different beam diameters.

As shown in Fig. 7, the output beam begins to appear non-Gaussian and asymmetric. The center of the beam moves left ($-\tilde{x}$ direction) as the beam diameter grows. As the diameter ($2w_x$) of the incident Gaussian beam increases, the output beam at $z = d + z_2$ also begins to develop greater asymmetry along the $+\tilde{x}$ direction. For Gaussian beam width $2w_x = 40$ mm, the asymmetrically-shaped output beam shows a peak at $\tilde{x} = -8$ mm, and the right side falls off more steeply than the left side.

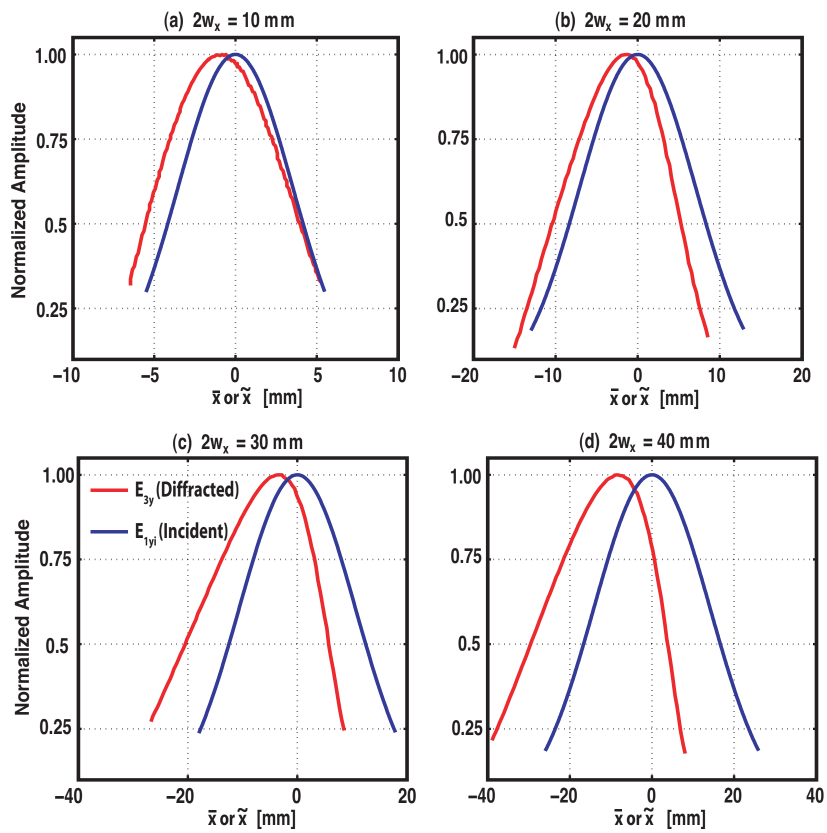

Fig. 7. Incident and first-order, forward-propagating diffracted waves as a function of $\hat{x}$ or $\tilde{x}$ at $z = -z_1$ and $z = d + z_2$. The incident Gaussian beam has $1/e^2$ diameter $2w_x$ and temporal full-width, half-maximum (FWHM) 33-ps ($\sigma_o = 27$ ps). The plots show different values of $2w_x$. Refractive indices for the three regions are $n_1 = n_3 = 1$ and $n_2 = 1.5$.

The output waveform $p_o(t)$ at different beam diameters is shown in Fig. 8. The curve labeled “Input” represents the reference and is the input pulse modulated onto the incident beam. All output pulses with different beam diameters are normalized by the average energy of the incident signal, $p_i(t)$. As seen in Fig. 8, the pulse width of the output pulse p_o increases as the Gaussian beam width w_x increases, while the peak amplitude reduces as the pulse spreads.

#106187 - $15.00 USD Received 9 Jan 2009; revised 20 Feb 2009; accepted 3 Mar 2009; published 24 Mar 2009

Because an HOE is not a true-time-delay device, this dispersion can affect the communication signal by broadening optical pulses beyond a bit slot. The bit period τ_b of the input pulse $p_i(t)$ is 100 ps for a 10-Gb/s rate. The output pulse is broadened to $2.5\tau_b$ at Gaussian beam diameter $2w_x = 30$ mm and to $3.0\tau_b$ at Gaussian beam diameter $2w_x = 40$ mm. The peak amplitude of the output pulse at beam diameter $2w_x = 40$ mm is reduced to 64% of the peak input amplitude.

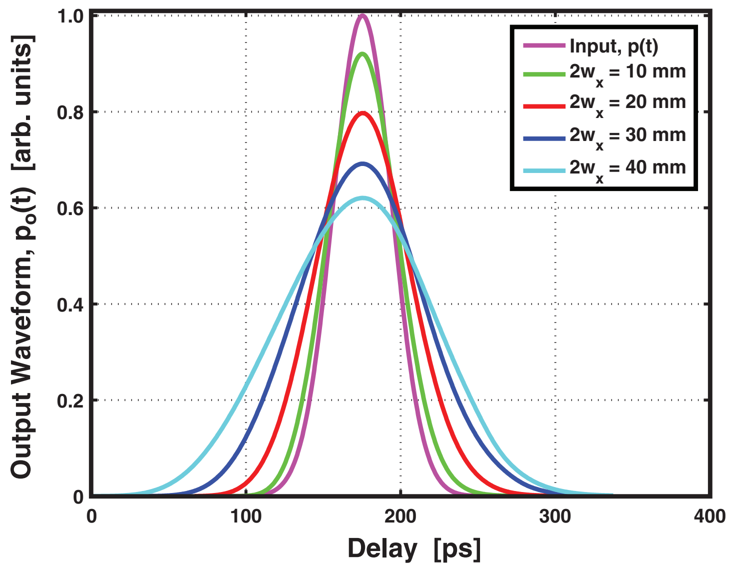

Fig. 8. Normalized output waveforms, p_o, for first-order, forward-propagating diffracted waves as a function of time at $z = z_1 + d + z_2$. The incident wave is a Gaussian beam with $1/e^2$ diameter $2w_x$ and a Gaussian temporal pulse with 33-ps FWHM ($\sigma_o = 27$ ps). $z_1 = 10w_x$ and $z_2 = 10w_x$

6. HOE simulation of communication performance

The configuration for the bit-error ratio (BER) simulations is shown in Fig. 9. A pattern generator produces a $2^{23} - 1$-bit pseudo-random-bit sequence with equal probability for occurrence of ones and zeros. The temporal waveform emitted by the HOE, $p_o(t)$, is pre-calculated using the method discussed in Sections 3 and 4 and the results shown in Section 5.

The incident beam in Region 1 is modulated by a Gaussian pulse and a return-to-zero, on-off-keyed (RZ-OOK) modulation format with 33% duty cycle. The bit rate is 10 Gbit/s. The amplitude of $p_o(t)$ is varied to change the average received power for the one bit. The encoded data-pulse train is described by $P(t)$.

$$P(t) = \sum_{n_b=1}^{N_b} \mathrm{Bit}(n_b) \times p_o(t - n_b\, \tau_b), \qquad \text{where} \quad \tau_b = 100 \text{ ps} \tag{37}$$

A bandwidth-limited, optically-preamplified receiver with gain value G is used as the optical receiver. Additive white Gaussian noise is applied to the received signal. The total noise is dominated by amplified spontaneous emission (ASE) noise from the pre-amplifier [10,11]. The variance in ASE noise for two polarizations is calculated in Eq. (38),

$$\sigma_N^2 = 2 \times n_{sp} \times h \times f \times B_o \times (G-1), \tag{38}$$

#106187 - $15.00 USD Received 9 Jan 2009; revised 20 Feb 2009; accepted 3 Mar 2009; published 24 Mar 2009

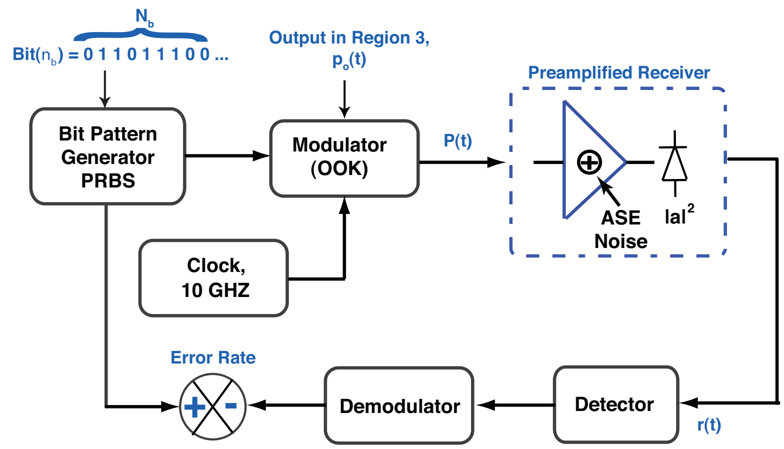

Fig. 9. Simulation approach for HOE bit-error-ratio analysis.

where n_{sp} is the spontaneous emission factor ($n_{sp} \geq 1$). h is Planck's constant; f is the center optical frequency (c/λ_o); and B_o is the combined amplifier and filter bandwidth. The received signal after optical detection is expressed in Eq. (39).

$$r(t) = \sum_{n_b=1}^{N_b} (\mathrm{Bit}(n_b) \times p_o(t - n_b\,\tau_b) + n_{ASE}(t))^2 \tag{39}$$

Maximum likelihood detection is used to classify the received signal as a zero or a one. Because of the receiver's square-law detection, the noise distributions for zeros and ones differ. The optimal threshold is computed based on the noise distribution for zeros and ones, at different transmitted powers. The signals are demodulated and compared with the transmitted pattern to determine bit errors.

7. Bit-error ratio simulation results

In this analysis we assume the size of the grating to exceed the beam spot size, simplifying the problem and neglecting edge effects and vignetting. Moreover, we assume ideal diffraction efficiency and only losses due to Fresnel reflections from mismatch between refractive indices ($n_1 = n_3 \neq n_2$). The spot diameter of the optical beam varies between 5 and 40 mm. The BER results for different beam diameters using the simulations discussed in Section 6 are shown in Fig. 10. The incident angle θ_1 is set to 33°, and we assume a wavelength λ_o of 1550 nm. The curve labeled "limit" is the quantum-noise-limited BER.

Because true-time delay is not implemented in the simulations, the pulse train experiences non-true-time-delay dispersion from diffraction. The power penalty due to the dispersion increases as the beam spot size increases. In the case of $2w_x = 40$ mm, the inter-symbol interference (ISI) introduced by the HOE appears to be the dominant factor in the power penalty. From Fig. 8(a), the output waveform p_o at $z = -z_1 + d + z_2$ is spread out into more than three bit slots.

The slope of the BER for $2w_x = 40$ mm differs from other cases as it requires more power to achieve low BER. The power penalty between $2w_x = 40$ mm and the reference BER curve labeled "limit" is 6 dB at a BER of 10^{-5}, while the power penalty for a BER of 10^{-3} is only 5 dB. The change of slope in BER is due to the stronger ISI present in the large-beam conditions.

#106187 - $15.00 USD Received 9 Jan 2009; revised 20 Feb 2009; accepted 3 Mar 2009; published 24 Mar 2009

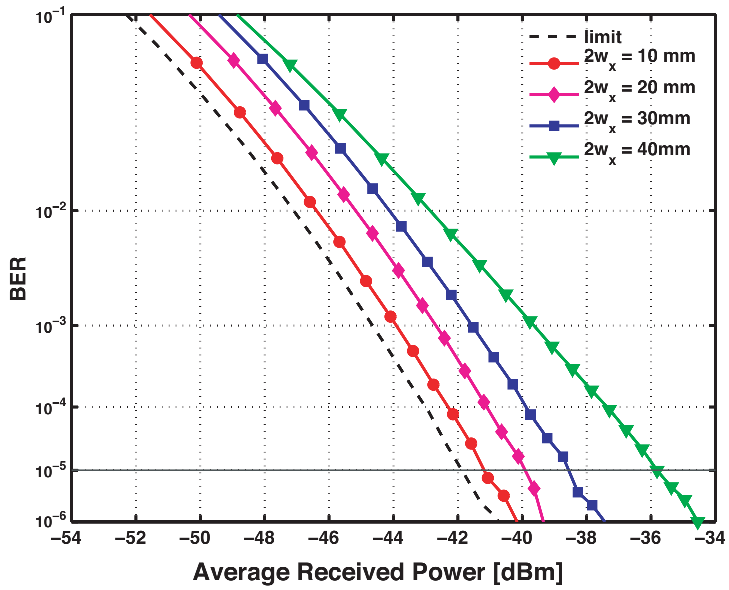

Fig. 10. Bit-error ratio (BER) of HOE for 10-Gb/s simulation (RZ-OOK). $\theta_1 = 33^o$ and $\lambda_o = 1550$ nm. Horizontal line shows a 10^{-5} BER.

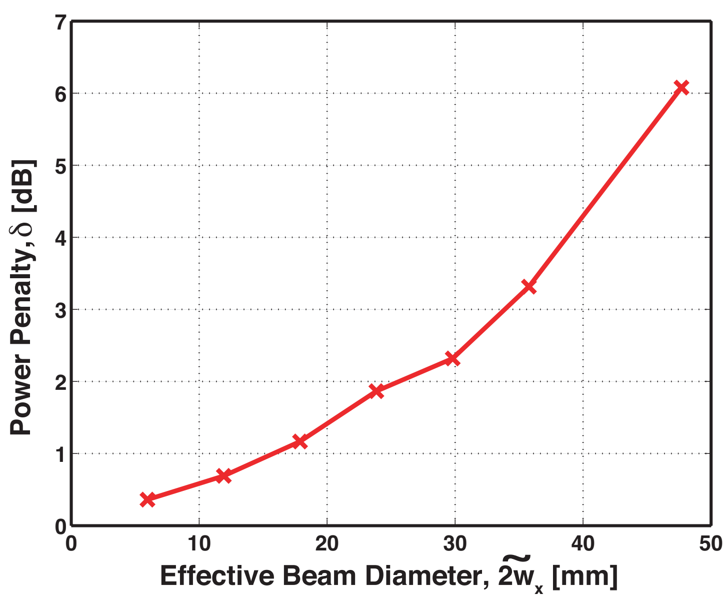

Fig. 11. Power penalty of the HOE as a function of effective beam diameter $\widetilde{2w_x}$, generalized for varying diffraction angle. $\lambda_o = 1550$ nm, BER $= 10^{-5}$, $\widetilde{2w_x} = \frac{2w_x}{\cos\theta}$.

The HOE power penalty depends on both incident angle and beam spot size. For a fixed spot size, we expect the power penalty to increase as incident angle θ_1 increases. We define an *effective beam spot diameter* ($\widetilde{2w_x}$) at the grating interface, that accounts for bending of the rays due to diffraction. This effective beam size is given by $\widetilde{2w_x} = \frac{2w_x}{\cos\theta_1}$. Various spot size and incident angle pairs that correspond to a fixed effective beam spot size are expected to yield the same power penalty. This technique allows us to extrapolate the results to HOE configurations with different diffraction angles and beam sizes. The plot in Fig. 11 shows the power penalty trend versus the effective beam diameter ($\widetilde{2w_x}$) at a 10^{-5} BER. The scaling applies best to the quasi-linear portion of the cosine function, where θ_1 remains between approximately 5 and 50°.

8. Summary and conclusions

In this work we adapt the coupled-wave equations to include a beam's spatial profile. We model the diffracted beam emitted by an HOE for a Gaussian incident beam, and include a temporal pulse envelope on the propagating beam. The results for HOE non-true-time-delay pulse broadening using a Gaussian temporal pulse are shown. As expected, this broadening increases with beam diameter. A data transmission model is developed to quantify power penalty due to the HOE pulse broadening. The BER simulation results show that for small effective beam diameters ($\widetilde{2w_x} \leq 30$ mm) the power penalty increases linearly as the diameter of the beam increases. However, for larger effective beam diameters, such as $\widetilde{2w_x} > 30$ mm, the power penalty increases more rapidly at low BER. From a diffraction efficiency standpoint, the beam diameter is lower-bounded by the spatial impulse response of the HOE. For the case of an HOE with grating period $\Lambda = 1420$ nm and $\theta_1 = 33°$, the beam diameter should exceed approximately 1 mm to have high diffraction efficiency. Finally, we expect the diffraction power penalty to increase for data rates above the 10-Gb/s rate studied here.

Acknowledgments

This work was sponsored by the Department of the Air Force under Air Force Contract FA8721-05-C-0002. Opinions, interpretations, conclusions, and recommendations are those of the authors and are not necessarily endorsed by the United States Government.

Jing M. Tsui acknowledges partial support by the National Science Foundation, grant CCF0649235.

#106187 - $15.00 USD Received 9 Jan 2009; revised 20 Feb 2009; accepted 3 Mar 2009; published 24 Mar 2009